Efficient and accurate simulation of two-phase relative permeability curves using the lattice Boltzmann method ⊘

Chun Li (李春) ⓘ ; Jieming Wang (王皆明); Youzhi Hao (郝有志) ⓘ ; Kun Tu (屠坤); Xin Lai (赖欣);
Haibo Huang (黄海波) ✉ ⓘ

Check for updates

View Online   Export Citation

Articles You May Be Interested In

Two-scale structure of the current layer controlled by meandering motion during steady-state collisionless driven reconnection

Phys. Plasmas (July 2004)

Efficient and accurate simulation of two-phase relative permeability curves using the lattice Boltzmann method

View Online   Export Citation   CrossMark

Chun Li (李春),[1,2] (iD) Jieming Wang (王皆明),[1,2] Youzhi Hao (郝有志),[3] (iD) Kun Tu (屠坤),[1,2] Xin Lai (赖欣),[1,2]
and Haibo Huang (黄海波)[3,a] (iD)

AFFILIATIONS

[1]PetroChina Research Institute of Petroleum Exploration and Development, Beijing 100083, China
[2]CNPC Key Laboratory of Underground Oil and Gas Storage Engineering, Langfang 065007, China
[3]Department of Modern Mechanics, University of Science and Technology of China, Hefei, Anhui 230026, China

[a]Author to whom correspondence should be addressed: huanghb@ustc.edu.cn

ABSTRACT

The steady-state method, commonly utilizing periodic boundary conditions and constant volume force, has long been employed to measure two-phase relative permeability using the lattice Boltzmann method (LBM). This study introduces the first application of LBM for unsteady-state measurement of two-phase relative permeability curves, removing the restrictions imposed by periodic boundaries. By comparing the results with steady-state measurements, we demonstrate that the proposed unsteady-state methods yield accurate relative permeability curves while significantly enhancing computational efficiency. We detail the process of determining the driving pressure (Δp) and initial flow rates (q) in unsteady simulations and analyze the characteristics of K_{ro} in these simulations. Our study suggests that, while K_{ro} should ideally be plotted as a function of saturation within the porous media (S_w), K_{rw}, calculated based on the flow at the exit, should be expressed as a function of S_{we} rather than S_w. To obtain an accurate K_{rw} curve, it is essential to discard spurious data from unsteady LBM simulations, particularly at higher S_w values approaching unity. Our findings show that both "constant-Δp" and "constant-q" unsteady simulations can produce satisfactory relative permeability curves. However, the constant-q method is more predictable, with the measured flow flux closely aligning with the specified value, making it more reliable and easier to manage. Overall, the unsteady-state method offers a robust and efficient framework for future numerical research on relative permeability measurement in porous media.

Published under an exclusive license by AIP Publishing. https://doi.org/10.1063/5.0277525

I. INTRODUCTION

The measurement of two-phase relative permeability is crucial for reservoir characterization and plays a vital role in optimizing oil recovery strategies. Relative permeability curves provide essential insights into the flow behavior of oil and water within porous media, influencing reservoir simulation, enhanced oil recovery (EOR) techniques, and production forecasting.[1] Accurate determination of these curves is fundamental to understanding multiphase flow dynamics and improving hydrocarbon extraction efficiency.

Two primary methods are used to measure relative permeability in rock samples: the steady-state method and the unsteady-state method. In both method, it is assumed that the two-phase fluids are immiscible and incompressible and the effects of capillary pressure and gravity are neglected. The steady-state method involves injecting oil and water simultaneously at a constant flow rate until equilibrium

is reached. At this point, fluid saturation and pressure stabilize, allowing direct calculation of relative permeability using Darcy's law. By varying the injection ratio, a series of relative permeability values at different saturations can be obtained, enabling the construction of relative permeability curves.[2]

In contrast, the unsteady-state method is based on the Buckley–Leverett theory of two-phase flow.[3] It begins by saturating the rock sample with water, followed by oil displacement to achieve irreducible water saturation. Waterflooding is then performed, and fluid production rates and pressure differences are recorded over time. The "J.B.N." method (Johnson–Bossler–Naumann) is used to calculate relative permeability from the experimental data, generating curves that reflect dynamic fluid displacement.[4] While the steady-state method is straightforward, the unsteady-state method better captures transient flow behavior, making it more representative of real reservoir conditions.

With the advent of advanced imaging technologies, such as X-ray computed tomography (CT), and the rapid development of computational capabilities, it has become possible to directly simulate fluid flow within digital rock cores. These digital representations of porous media, reconstructed from high-resolution CT scans, enable detailed analysis of pore-scale phenomena and provide a bridge between laboratory experiments and field-scale applications. This progress has opened new avenues for understanding multiphase flow dynamics and validating experimental results through numerical simulations.

Among computational methods, the lattice Boltzmann method (LBM) has emerged as a powerful tool for simulating multiphase flow in porous media.[5–11] As a mesoscopic method, LBM excels in handling complex wall geometries and is inherently explicit, making it highly parallelizable. Unlike traditional macroscopic schemes, LBM does not require solving the Poisson equation, significantly improving computational efficiency.

Among the various multiphase LBM models, the Rothman and Keller (R–K) model stands out for its accuracy.[5] Initially proposed by Rothman and Keller[12] and further refined by Gunstensen et al.,[13] the R–K model incorporates an additional binary fluid collision term into the Lattice Boltzmann equation.[13] Latva-Kokko and Rothman[14] later improved the recoloring step, reducing lattice pinning effects and spurious currents.[15,16] Reis and Phillips[17] developed a two-dimensional nine-velocity R–K model, which accurately accounts for surface tension in the Navier–Stokes (N–S) equations.

The R–K model simplifies the implementation of wetting conditions by allowing the specification of fluid densities at solid nodes, unlike the free-energy LBM, which requires imposing density gradients near walls. This simplicity has facilitated its application in porous media simulations.[8,18] Additionally, the use of the multiple-relaxation-time (MRT) collision model,[19] in the R–K method has significantly reduced spurious currents and improved numerical stability, making it suitable for simulating capillary fingering phenomena in two-phase flow.[20]

Therefore, the color-gradient (Rothman–Keller) LBM is widely used for multiphase flow simulations due to its simplicity, robustness, and ability to maintain sharp interfaces with relatively low spurious velocities.[5] It supports large viscosity ratios and ensures good numerical stability, making it suitable for simulating complex porous media. Furthermore, it allows independent control over interfacial tension and wettability. However, it lacks full thermodynamic consistency compared to free-energy or pseudopotential models and has limited ability to handle very high-density ratios, which may affect some applications.

In the literature, LBM simulations of relative permeability under steady-state conditions often rely on periodic boundary conditions, which assume an infinitely long porous medium in the flow direction. This setup can lead to unphysical results, such as slightly negative relative permeability values.[11,21,22] To address this, non-periodic boundary conditions have been explored. For instance, Huang et al.[23] simulated two-phase immiscible displacements under constant pressure differences, but the pressure outlet boundary condition showed limitations, such as severe droplet deformation near the outlet.

In our previous work,[24] we developed LBM simulations for steady-state relative permeability measurements using convective outflow and inlet constant flux boundary conditions. We investigated the effects of wettability, initial saturation, viscosity ratio, capillary number,

and micro two-phase distribution on permeabilities. The study highlighted the importance of free outflow boundary conditions at the outlet, which automatically determine phase distributions.[25,26] These boundary conditions are also applied in the current study.

Although the LBM has been applied to simulate two-phase relative permeability under steady-state conditions, there is a lack of systematic studies on using LBM for unsteady-state simulations to extract relative permeability curves. To our knowledge, no prior work has demonstrated unsteady-state relative permeability measurements within the LBM framework. In practice, unsteady-state methods are often significantly more efficient than steady-state approaches, especially for high-resolution simulations in complex porous structures, making them highly attractive for practical applications.

In this work, we focus on unsteady-state simulations of two-phase relative permeability curves using LBM. By leveraging the strengths of the R–K model and advanced boundary conditions, we aim to enhance the understanding of dynamic oil–water interactions in porous media, contributing to more accurate reservoir characterization and improved oil recovery strategies. The paper is organized as follows: First, we introduce the R–K model and convective outflow boundary conditions, followed by validation through benchmark problems. Next, we present simulations in a 400×400 porous medium, comprehensively investigating unsteady LBM simulations for relative permeability under constant-pressure and constant-flow-rate conditions.

A. R–K model

In the Rothman–Keller (R–K) model, the particle distribution function (PDF) for fluid k is denoted as f_i^k. For two-phase flows, two separate distribution functions are defined: f_i^b and f_i^r, where b and r represent the "blue" and "red" components, respectively. The total PDF at a given position $\mathbf{x}$ and time t is then given by $f_i(\mathbf{x}, t) = \sum_k f_i^k(\mathbf{x}, t)$.

The Lattice Boltzmann Method (LBM) typically involves two primary steps: collision and streaming. However, in the R–K model, three steps are involved for each component: streaming, collision, and recoloring. Suppose an iteration begins with the streaming step. We now describe how these three steps form a loop. The streaming step is given by[17]

$$f_i^k(\mathbf{x} + \mathbf{e}_i\Delta t, t + \Delta t) = f_i^{k+}(\mathbf{x}, t), \tag{1}$$

where f_i^{k+} represents the PDF after the recoloring step. In this equation, $\mathbf{e}_i$ ($i = 0, 1, \ldots, b$) are the discrete velocities in the velocity model. For the D2Q9 velocity model (with $b = 8$), the nine discrete velocities are defined as

$$\mathbf{e}_i = \begin{cases} (0, 0) & \text{for } i = 0, \\ \left(\cos\left[(i-1)\frac{\pi}{2}\right], \sin\left[(i-1)\frac{\pi}{2}\right]\right)c & \text{for } i = 1, 2, 3, 4, \\ \left(\sqrt{2}\cos\left[(i-5)\frac{\pi}{2} + \frac{\pi}{4}\right], \right. \\ \left. \sqrt{2}\sin\left[(i-5)\frac{\pi}{2} + \frac{\pi}{4}\right]\right)c & \text{for } i = 5, 6, 7, 8. \end{cases} \tag{2}$$

Here, c represents the lattice speed, defined as $c = \frac{\Delta x}{\Delta t}$, where Δx is the lattice spacing and Δt is the time step. In our study, we use lattice

units where $1\,\mathrm{lu} = 1\,\Delta x$, $1\,\mathrm{ts} = 1\,\Delta t$, and the mass unit is denoted as mu.

The collision step can be written as[14]

$$f_i^{k*}(\mathbf{x}, t) = f_i^k(\mathbf{x}, t) + (\Omega_i^k)^1 + (\Omega_i^k)^2, \tag{3}$$

where $f_i^{k*}(\mathbf{x}, t)$ is the post-collision state. There are two collision terms in the equation, i.e., $(\Omega_i^k)^1$ and $(\Omega_i^k)^2$. If the lattice Bhatnagar–Gross–Krook (BGK) scheme is adopted, the first collision term is

$$(\Omega_i^k)^1 = -\frac{\Delta t}{\tau}\left(f_i^k(\mathbf{x}, t) - f_i^{k,eq}(\mathbf{x}, t)\right), \tag{4}$$

where τ is the relaxation time.

The equilibrium distribution function $f_i^{k,eq}(\mathbf{x}, t)$ can be calculated using[17]

$$f_i^{k,eq}(\mathbf{x}, t) = \rho_k\left(C_i + w_i\left[\frac{\mathbf{e}_i \cdot \mathbf{u}}{c_s^2} + \frac{(\mathbf{e}_i \cdot \mathbf{u})^2}{2c_s^4} - \frac{(\mathbf{u})^2}{2c_s^2}\right]\right), \tag{5}$$

where the density of the kth component is

$$\rho_k = \sum_i f_i^k, \tag{6}$$

and the total density is $\rho = \sum_k \rho_k$. The momentum is

$$\rho\mathbf{u} = \sum_k \sum_i f_i^k \mathbf{e}_i. \tag{7}$$

In the above formula, the coefficients are defined as follows:[17] $C_0 = \alpha_k$, $C_i = \frac{1-\alpha_k}{5}$ for $i = 1, 2, 3, 4$, and $C_i = \frac{1-\alpha_k}{20}$ for $i = 5, 6, 7, 8$, where α_k is a parameter that adjusts the fluid density.[17,27] For simplicity, α is assumed to be identical for both fluid components, i.e., $\alpha_r = \alpha_b = \frac{4}{9}$. The initial densities of the red and blue fluids are considered identical $\rho_{ri} = \rho_{bi} = \frac{5}{9}$, which is a reasonable assumption since the densities of water and oil are close in value. It is important to note that when $\alpha_r = \alpha_b = \frac{4}{9}$, Eq. (5) reduces to the standard formula used in single-phase LBM. The other parameters are as follows: $w_0 = \frac{4}{9}$, $w_i = \frac{1}{9}$ for $i = 1, 2, 3, 4$, and $w_i = \frac{1}{36}$ for $i = 5, 6, 7, 8$.

The viscosity of each component is given by $\nu_k = c_s^2(\tau_k - 0.5)$, where $c_s^2 = \frac{1}{3}c^2$. The viscosity ratio is defined as $M = \frac{\nu_{nw}}{\nu_w}$, where the subscripts "nw" and "w" refer to the non-wetting and wetting fluids, respectively. The R–K LBM is a diffusion–interface method. Due to the diffusion, an interface region exists between the two components. The viscosity in this interface region can be determined by

$$\nu = \frac{\rho}{\frac{\rho_r}{\nu_r} + \frac{\rho_b}{\nu_b}}. \tag{8}$$

This formula is also applicable in the regions of pure red or blue components. Accordingly, the relaxation time at a lattice node $\mathbf{x}$ can be determined by

$$\tau = \frac{\nu}{c_s^2} + 0.5. \tag{9}$$

The second collision term is more complex and there are some different forms found in the literature.[11,17] An example is[11]

$$(\Omega_i^k)^2 = \frac{A}{2}|\mathbf{f}|(2 \cdot \cos^2(\lambda_i) - 1), \tag{10}$$

where λ_i is the angle between the color gradient $\mathbf{f}$ and the direction $\mathbf{e}_i$, and we have $\cos(\lambda_i) = \frac{\mathbf{e}_i \cdot \mathbf{f}}{|\mathbf{e}_i| \cdot |\mathbf{f}|}$. Here, A is correlated with surface tension, i.e.,

$$A = 9\sigma/(2\tau\rho_{ri}). \tag{11}$$

The color-gradient $\mathbf{f}(\mathbf{x}, t)$ is calculated as[14]

$$\mathbf{f}(\mathbf{x}, t) = \sum_i \mathbf{e}_i \sum_j \left[f_j^r(\mathbf{x} + \mathbf{e}_i\Delta t, t) - f_j^b(\mathbf{x} + \mathbf{e}_i\Delta t, t)\right]. \tag{12}$$

However, according to the study of Reis and Phillips,[17] the correct collision operator should be

$$(\Omega_i^k)^2 = \frac{A}{2}|\mathbf{f}|\left[w_i\frac{(\mathbf{e}_i \cdot \mathbf{f})^2}{|\mathbf{f}|^2} - B_i\right], \tag{13}$$

where $B_0 = -\frac{4}{27}$, $B_i = \frac{2}{27}$, $i = 1, 2, 3, 4$, $B_i = \frac{5}{108}$, $i = 5, 6, 7, 8$. Using these parameters, the correct term due to surface tension in the N–S equation can be recovered.[17]

Then, the recoloring step is implemented to achieve separation of the two fluids[14]

$$f_i^{r,+} = \frac{\rho_r}{\rho}f_i^* + \beta\frac{\rho_r\rho_b}{\rho^2}f_i^{(eq)}(\rho, 0)\cos(\lambda_i), \tag{14}$$

$$f_i^{b,+} = \frac{\rho_b}{\rho}f_i^* - \beta\frac{\rho_r\rho_b}{\rho^2}f_i^{(eq)}(\rho, 0)\cos(\lambda_i), \tag{15}$$

where $f_i^* = \sum_k f_i^{k*}$.

After updating $f_i^r(\mathbf{x}, t)$ and $f_i^b(\mathbf{x}, t)$, the streaming step [i.e., Eq. (1)] should be applied to each component. By iterating through the procedure outlined above, two-phase flow simulations can be conducted.

In the model, A and β are the two key parameters that control interfacial properties. While β does not affect surface tension directly, it influences the interface thickness, isotropy, and the magnitude of spurious currents.[20] In our simulations, β is typically set to 0.7.[20] The pressure in the flow field is obtained from the density using the equation of state $p = c_s^2\rho$.

For two components with identical densities, the equilibrium distribution function (DF) remains the same. Consequently, it is not necessary to calculate the collision steps—Eqs. (4) and (13)—separately for each component. The two collision steps can therefore be combined as follows:

$$(\Omega_i)^1 = -\frac{\Delta t}{\tau}\left(f_i(\mathbf{x}, t) - f_i^{eq}(\mathbf{x}, t)\right) \tag{16}$$

and

$$(\Omega_i)^2 = A|\mathbf{f}|\left[w_i\frac{(\mathbf{e}_i \cdot \mathbf{f})^2}{|\mathbf{f}|^2} - B_i\right], \tag{17}$$

where $f_i = \sum_k f_i^k$.

B. Contact angle

To account for the effect of wettability on relative permeability, the contact angle at the pore scale must be specified. This is achieved by setting the values of ρ_r and ρ_b at the wall nodes, denoted as ρ_r' and ρ_b', respectively, which allows for the specification of different contact

angles. The contact angle θ can be analytically determined using the following formula:[14]

$$\theta = \arccos\left(\frac{\rho_r' - \rho_b'}{\rho_{ri}}\right), \tag{18}$$

where θ is measured with respect to the red phase (water). By adjusting ρ_r' and ρ_b', the wettability of the wall can be controlled, as these parameters influence the color gradient near the wall, as described in Eq. (12).

C. Boundary conditions

We will now introduce the inlet velocity (or pressure) boundary condition and the outlet natural convective (flow-out) boundary condition. First, the velocity inlet boundary condition and constant pressure (or density) boundary condition applied to the upper inlet boundary are discussed.

For the upper velocity boundary condition, the distribution functions f_4, f_7, f_8 are unknown after the streaming step for both the majority and minor components. Using the non-equilibrium bounce-back assumption,[28] the density of the majority component at the inlet boundary (assuming the inlet velocity u_i is specified) can be calculated as

$$\rho_n = \frac{f_0^n + f_1^n + f_3^n + 2(f_2^n + f_5^n + f_6^n)}{1 + u_i}. \tag{19}$$

The unknown distribution functions can then be determined as follows:[28]

$$f_4^n = f_2^n - \frac{2}{3}\rho_n u_i,$$
$$f_7^n = f_5^n + \frac{1}{2}(f_1^n - f_3^n) - \frac{1}{6}\rho_n u_i, \tag{20}$$
$$f_8^n = f_6^n + \frac{1}{2}(f_3^n - f_1^n) - \frac{1}{6}\rho_n u_i.$$

This velocity boundary condition can also be applied to the minor component.

If we wish to apply the pressure boundary condition (assuming ρ_n has been specified) at the top inlet boundary, the procedure is similar to the velocity boundary condition, but Eq. (19) is modified as follows:

$$u_i = \frac{f_0^n + f_1^n + f_3^n + 2(f_2^n + f_5^n + f_6^n)}{\rho_n} - 1. \tag{21}$$

Then, the same equations for the unknown distribution functions in Eq. (20) are applied.

Next, for single-phase flow, pressure boundary conditions for the lower boundary can be handled similarly to the upper boundary. This involves determining the unknowns $f_2, f_5,$ and f_6.[28] However, for two-phase flow, it is challenging to determine whether a lattice node on the outlet is occupied by the red or blue component. A reasonable approach may be to perform an extrapolation. For example, if a node one or two layers above the bottom boundary is occupied by the red component, it can be assumed that the node at the boundary will also be occupied by the red component. In this case, the red fluid density is specified for that node, and the minor component's density is specified

for the other fluid. However, this simple extrapolation may introduce significant errors.

For the lower outflow boundary condition, a convective boundary condition is applied,[25,26] which is expressed as

$$\frac{\partial\chi}{\partial t} + U_i\frac{\partial\chi}{\partial y} = 0, \tag{22}$$

where U_i is the convective velocity and χ represents any physical variable used in the simulations.[26] In our simulations at the outlet ($j = 1$), the convective velocity at the lattice node (i, j) is specified as the value in the upper neighboring layer, i.e., $U_i = u_y(i, j + 1)$.

In the layer $j = 1$, assuming that $\chi = f_i$ when using the upwind scheme, we obtain the following equation:

$$\frac{f_k^n(j) - f_k^{n-1}(j)}{\Delta t} + U_i\frac{f_k^n(j + 1) - f_k^n(j)}{\Delta y} = 0 \quad \text{for} \quad U_i < 0. \tag{23}$$

This yields the solution

$$f_k^n(j) = \frac{\frac{\Delta y}{\Delta t}f_k^{n-1}(j) - U_i f_k^n(j + 1)}{\frac{\Delta y}{\Delta t} - U_i}, \tag{24}$$

where $k = 0, 1, 2, \ldots, 8$ and $j = 1$. On the other hand, if $U_i > 0$ and the upwind scheme is applied, this implies that information is flowing from outside the domain into the domain. Since the external information is unknown, we set $U_i = 0$ for this case. Therefore, the boundary condition becomes

$$f_k^n(j) = f_k^{n-1}(j) \quad \text{for} \quad U_i > 0. \tag{25}$$

The accuracy of the natural convection (flow-out) boundary condition has been extensively tested in Ref. 24.

D. Validation

To validate our numerical method, we simulated a non-wetting fluid (blue) displacing wetting fluid process (see Fig. 1) and compared the results with experimental data (yellow lines) from Ref. 29. The porous medium in the experiment consists of uniformly sized cylinders with irregular spacing (see Fig. 1). The physical parameters of the porous medium, as well as those of the wetting and non-wetting fluids used in the experiment, are listed in the rightmost column of Table I, alongside the corresponding simulation parameters.

In the simulation, the porous medium is discretized using a 600×600 lu domain, with each cylindrical obstacle having a diameter of 42 lu. The resulting porosity is 0.59. Both fluids (wetting and non-wetting) are assigned a density of $\rho_a = \frac{5}{9}\,\text{lu}^2/\text{ts}$, with initial densities at solid nodes set to $\rho_r = 0.4\,\text{lu}^2/\text{ts}$ and $\rho_b = 0.0\,\text{lu}^2/\text{ts}$, yielding a contact angle of $\sim 40°$ [see Eq. (18)]. The relaxation times are set to $\tau_r = 2.0$, $\tau_b = 0.7$, giving both fluids identical viscosities. A surface tension is set as $\sigma = 0.05\,\text{mu/ts}^2$.

In the simulation, the viscosity ratio μ_{non}/μ_w is ~ 0.135, whereas in the experiment it is much lower, around 0.0053. Another key parameter is the capillary number, defined at the pore scale as $Ca = \frac{\mu_w b^2 U_0}{k\sigma}$, where U_0 is the average inlet velocity. The simulated Ca is $\sim 5.8 \times 10^{-2}$, compared to 2.6×10^{-5} in the experiment. While using a higher Ca in simulations reduces computational cost, it can still
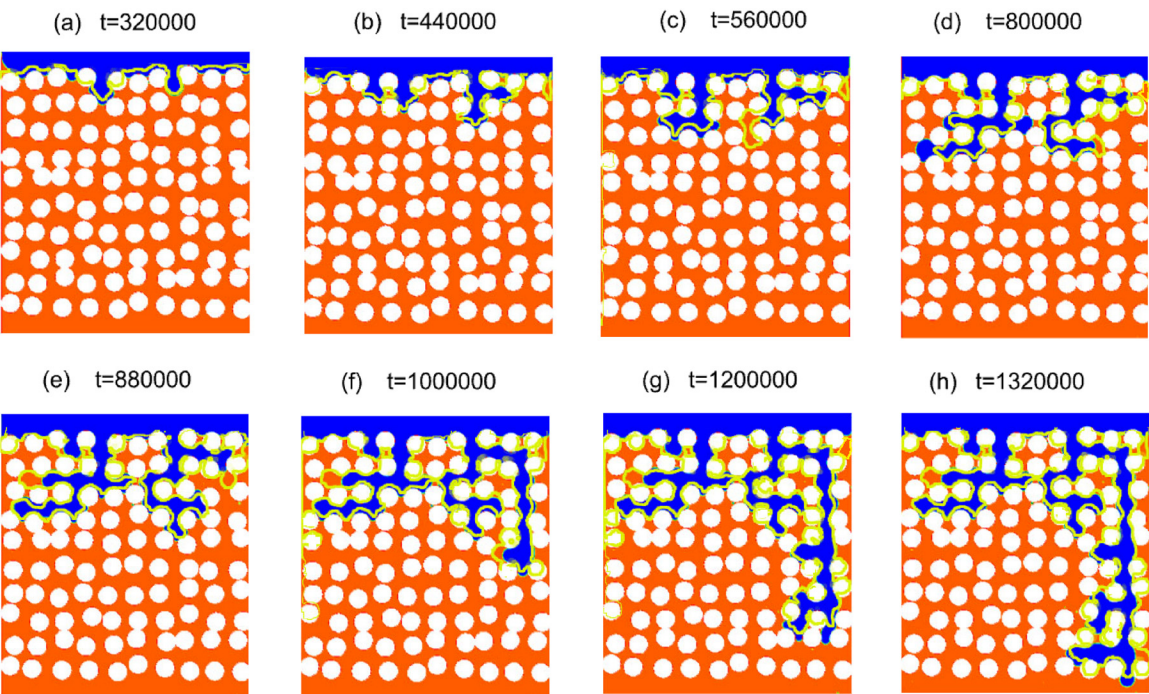
FIG. 1. Evolution of the two-phase flow in a porous medium. Comparison between the LBM results and experimental observations (yellow lines denote fluid interfaces) from Ref. 29. Initially, the porous medium is fully saturated with the wetting phase (red), which is then displaced by an invading non-wetting fluid (blue).

TABLE I. Geometrical parameters and fluid properties in the LB simulation and experiment.

	Symbol	Simulation	Experiment
Model length	L	600	30 mm
Model width	W	600	30 mm
Obstacle diameter	b	42	2 mm
Porosity	ϕ	≈ 0.59	≈ 0.59
Single-phase permeability	k	≈ 17	2.1×10^{-4} cm^2
Contact angle	θ_w	$\approx 40°$	$< 70°$
Wetting fluid viscosity	μ_w	0.278	3.6×10^{-3} Pa s
Non-wetting fluid viscosity	μ_{nw}	3.7×10^{-2}	1.9×10^{-5} Pa s
Wetting fluid density	ρ_w	0.5556	1.10×10^3 kg m^{-3}
Non-wetting fluid density	ρ_{nw}	0.5556	1.2 kg m^{-3}
Surface tension	σ	0.05	$\approx 6.2 \times 10^{-2}$ N m^{-1}
Capillary number	Ca	$\approx 5.8 \times 10^{-2}$	$\approx 2.6 \times 10^{-5}$

capture relevant flow features. According to the phase diagram in Ref. 30, viscous fingering occurs over a broad range in the M-Ca parameter space, particularly at low values of both, e.g., $M \sim O(10^{-1})$ and $Ca \sim O(10^{-2})$. Despite the higher Ca in our simulation, the resulting flow pattern remains consistent with viscous fingering, enabling meaningful comparison with the experimental results.

In the experiment, non-wetting fluid invasion is driven by a constant rate. In the simulation, we apply a constant inlet velocity

boundary condition with $U_a = 10^{-4}$ lu/ts at the top boundary, and an outflow boundary condition at the bottom. Initially, the non-wetting fluid occupies at least 10 lattice layers near the inlet. As shown in Fig. 1, the phase distributions from our LBM simulation [blue/red interfaces in panels (a)–(h)] closely match those from the experiment [yellow lines in panels (a)–(h)], confirming the accuracy of our simulation setup and validating the numerical method and the effectiveness of the convective boundary condition.
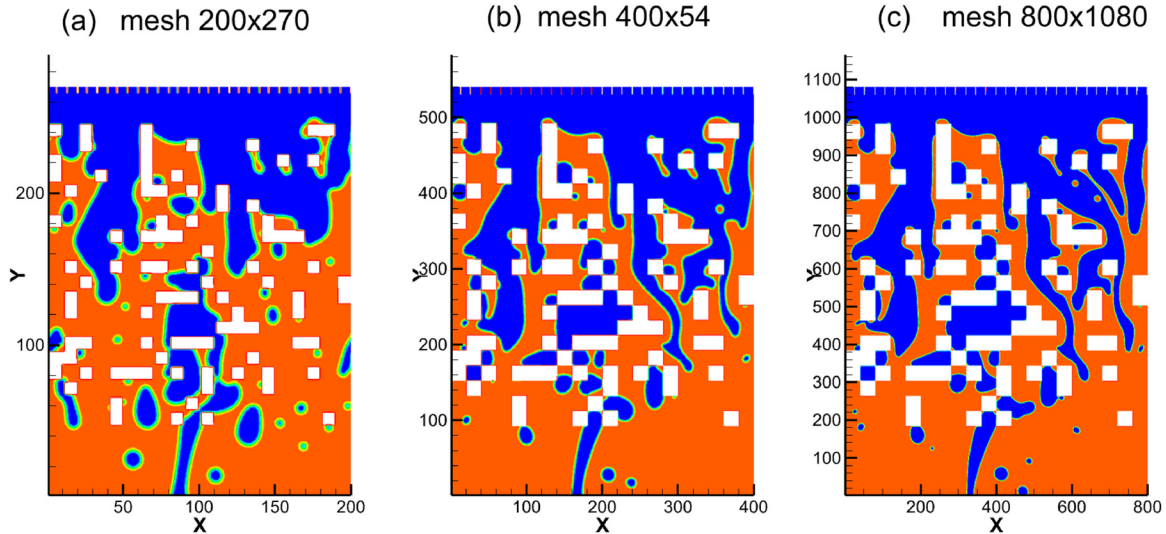
FIG. 2. Comparison of oil–water phase distributions for three different grid resolutions: 200×270, 400×540, and 800×1080 in (a)–(c) at dimensionless time $t^* = \frac{t}{L/U_a} = 0.375$.
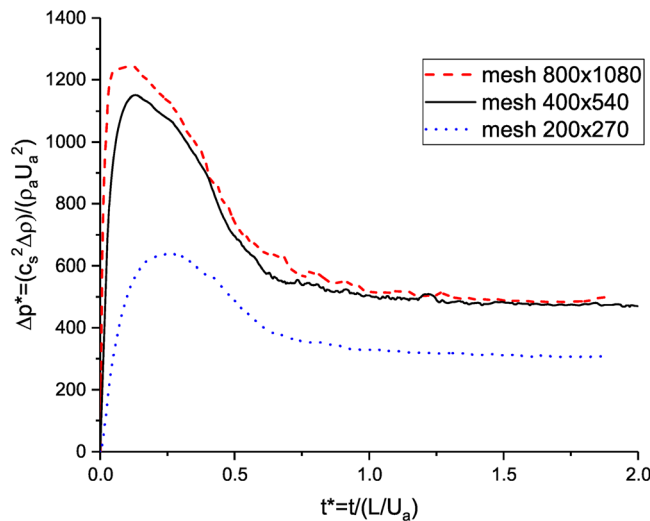

FIG. 3. Evolution of dimensionless pressure drop between the inlet and outlet over time for three grid resolutions: 200×270, 400×540, and 800×1080.

To evaluate mesh independence, we conducted simulations using three different grid resolutions: 200×270, 400×540, and 800×1080. These grids were applied to the same porous medium model to assess the sensitivity of simulation results to spatial resolution.

The initial condition represents a post-oil-displacement scenario in which a small amount of residual water remains. Subsequently, water is injected from the top of the domain to displace the remaining oil. The porous medium is specified to be oil-wet, characterized by a contact angle of $45°$, and the oil-to-water viscosity ratio is set to 2:1. Water is injected at a constant flux of $q = U_a L = 1.5 \, \text{lu}^2/\text{ts}$.

To ensure consistent flow regimes across all simulations, we maintained the same Reynolds number, defined as $Re = \frac{U_a L}{\nu} = \frac{q}{\nu}$, by keeping the oil and water viscosities constant. To ensure the capillary number, $Ca = \frac{U_a \mu}{\sigma}$, remained consistent as well, we adjusted the oil–water interfacial tension accordingly: $\sigma = 0.006$, 0.003, and 0.0015 for the coarse, medium, and fine grids, respectively.

Figure 2 presents the oil–water phase distributions at a common dimensionless time, $t^* = \frac{t}{L/U_a} = \frac{40000}{400/(1.5/400)} = 0.375$, for all three grid resolutions. The results from the coarse grid (200×270) differ significantly from those of the finer grids, indicating insufficient spatial resolution. In contrast, the phase distribution obtained with the medium-resolution grid (400×540) closely matches that of the high-resolution case (800×1080), demonstrating that the 400×540 grid is sufficient to accurately capture the key flow features.

We also monitored the dimensionless pressure drop across the domain throughout the simulations. Figure 3 presents the evolution of this pressure drop over time. The pressure curves for the medium and fine grids are in excellent agreement, while the coarse grid shows noticeable deviation. This further supports the conclusion that the 400×540 grid provides a good balance between accuracy and computational efficiency, and is therefore adopted for all subsequent simulations in this study.

II. RESULTS AND DISCUSSION
A. Steady-state measurement

The theoretical foundation for determining oil–water relative permeability using the steady-state method is based on the one-dimensional Darcy's law for fluid flow. Our LBM simulations follow this experimental procedure.

First, irreducible water saturation is established. This is done using the oil displacement method, where the oil phase is injected at a low flow rate to displace the water phase. The displacement rate is

then gradually increased until no more water is produced, indicating the formation of irreducible water saturation.

Next, the oil phase permeability of the rock sample under irreducible water saturation is measured. With a constant total flow rate, oil and water are injected simultaneously into the rock sample at a specified flow ratio. Once the inlet and outlet pressures stabilize and the oil and water flow rates become steady, the water saturation in the rock sample reaches equilibrium. At this point, the distribution of oil and water within the rock's pores becomes uniform, signifying a steady-state condition. The effective permeability of oil and water remains constant under these conditions.

By measuring the inlet and outlet pressures, as well as the oil and water flow rates, the effective permeability and relative permeability of oil and water can be directly calculated using Darcy's law. Varying the injection flow ratio of oil (q_o) and water (q_w) allows for the determination of oil–water relative permeability at different water saturations. These data are then used to plot the oil–water relative permeability curve for the rock sample.

The oil–water relative permeability using the steady-state method is calculated as follows:

$$K_{we} = \frac{q_w \mu_w L}{A \Delta p}, \quad K_{oe} = \frac{q_o \mu_o L}{A \Delta p}, \quad (26)$$

where Δp is the pressure difference between the inlet and outlet, L is the length of test section, A is the cross-sectional area, and K_{we} and K_{oe} are effective permeabilities of water and oil, respectively.

Then, the relative permeabilities of water and oil, K_{rw} and K_{ro}, respectively, can be calculated as follows:

$$K_{ro} = \frac{K_{oe}}{K_o(S_{ws})}, \quad K_{rw} = \frac{K_{we}}{K_o(S_{ws})}, \quad (27)$$

where S_{ws} is the irreducible water saturation.

The porous media simulated in our study consists of a 400×400 grid, totaling $160\,000$ grid points, with $\sim 123\,600$ pore lattice points, resulting in a porosity of $\phi = 77.25\%$. To facilitate calculations and the implementation of boundary conditions, blank grids were added to the upper and lower edges of the porous domain. The entire computational domain is 540×400, with the porous medium positioned between $Y = 90$ and $Y = 490$. This region is used to automatically calculate saturation during the simulation. The pressure statistics for the inlet and outlet are located at $Y = 520$ and $Y = 80$, near the upper and lower boundaries of the porous medium.

The absolute permeability of the porous media, K, is calculated using the following data. In our LBM simulation, we assume a single-phase flow with $\rho = \frac{5}{9}$, injected at a rate of $q = 1.56$ lu^2/ts into the porous medium. The fluid viscosity is $\nu = c_s^2(\tau - 0.5) \Delta t = 0.1667$. At steady state, the measured pressure difference is $\Delta p = c_s^2 \Delta \rho = \frac{1}{3} \times 0.00986 = 0.00328$. Using Darcy's law, the permeability is given by

$$K = \frac{\rho \nu L q}{A \Delta p} = \frac{\frac{5}{9} \times 0.1667 \times 440 \times 1.56}{400 \times 0.00328} = 48.4\,\text{lu}^2.$$

In our two-phase flow simulations, we consider only density-matched cases, with both water and oil having densities of $\frac{5}{9}$ mu/lu^2. Assuming that the kinetic viscosities of the two fluids are different, we set the relaxation times in the LBM as $\tau_o = 2$ for oil and $\tau_w = 1$ for water. Consequently, the kinetic viscosity of oil is $\nu_o = c_s^2(\tau_o - 0.5) \times \Delta t = 0.5$ lu^2/ts, and the kinetic viscosity of water is $\nu_w = c_s^2 \times (\tau_w - 0.5)\Delta t = 0.1666$ lu^2/ts. The oil–water interfacial tension is set as $\sigma = 0.003$ mu/ts^2.

In our steady-state measurements, the total flow rate is kept constant. Oil and water are simultaneously injected into the porous medium at a constant rate with a specific velocity: $u = 0$ and $v = -0.004$ lu/ts. To mimic the actual experimental setup, 30 short, identical narrow channels are set at the inlet, with either oil or water injected into each channel. A velocity-in boundary condition is applied at the top layer of the simulation, where $u = 0$ and $v = -0.004$ lu/ts at each lattice node. Meanwhile, a natural flow-out boundary condition is applied at the bottom boundary.

Regarding the wettability of the porous media and the inlet short channels, we assume that these solid nodes are oleophilic, meaning the contact angle of the oil phase is less than 90 degrees. The "wall densities" for water and oil are set as $\rho'_w = 0.0$ and $\rho'_o = 0.2777$, respectively. According to Eq. (18), the contact angle of water is calculated as

$$\theta = \cos^{-1}\left(\frac{0 - 0.2777}{0.5555}\right) \approx 120°.$$

This represents a hydrophobic case. In all cases presented in this paper, the wettability is fixed.

Our simulations are initialized under the condition where the pores are partially saturated with irreducible water, with the remaining pore space occupied by oil. Specifically, we first use oil to displace the water in the porous medium, leaving only the irreducible water. This configuration is then used as the initial state, after which oil or water is injected into the 30 small channels at the inlet.

To allocate different flow rates, we distribute the oil and water across the 30 channels. For example, oil is injected into 5 channels, while water is injected into the remaining 25. The corresponding water saturation is roughly estimated as $\frac{25}{30}$, or $\sim 84\%$. However, this is an estimate, and the final saturation distribution may differ slightly due to the viscous coupling effect between the two phases. It is important to note that, when injecting oil into 5 of the channels, we aim to distribute these inlets as evenly as possible across the inlet regions. This ensures that the oil and water phases have the opportunity to mix fully before entering the pores.

Once the flow reaches a steady state, we measure the average pressures of the two phases at positions $Y = 80$ and $Y = 520$. Using the pressure difference between these two points and applying Darcy's law, we can calculate the corresponding relative permeability. The distribution of the two phases in the pores at steady state for several typical cases is shown in Fig. 4. The relative permeability permeabilities for the 11 cases are presented in Fig. 5 (indicated by discrete circles and disks).

We observe that some cases, despite having very similar saturations (e.g., two cases at $S_w \approx 0.43$), exhibit noticeable variations in their relative permeability values. To better understand this, let us conduct a simple analysis.

As discussed in Ref. 24, even with the same injection ratio, the distribution of phases across the 30 channels can significantly affect the relative permeability.

To evaluate the impact of two-phase distribution at the inlet, we performed two simulation cases (Cases A and B) with identical oil–water injection ratios at the inlet. The phase distributions at the top of
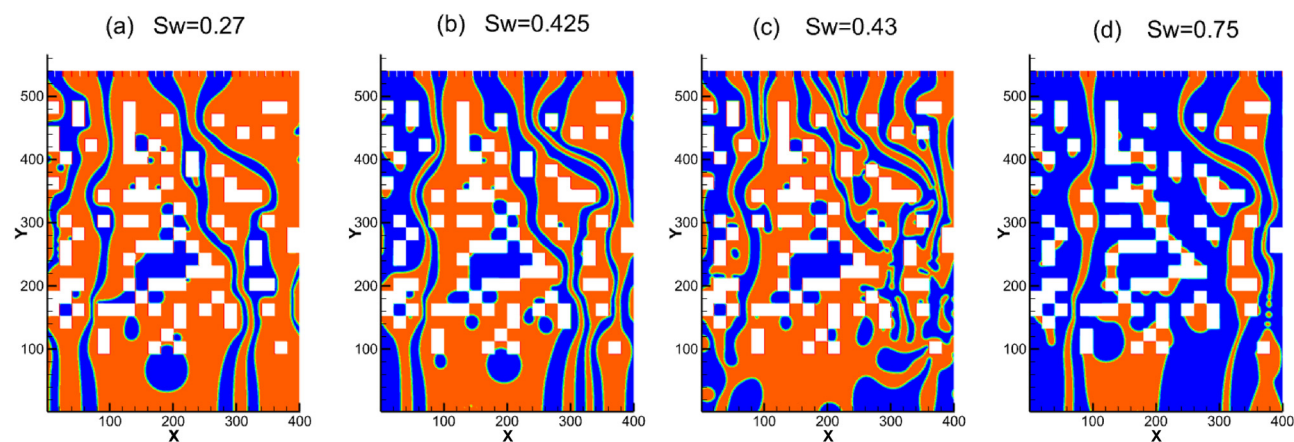
FIG. 4. Measuring the relative permeability using steady flow method. Two-phase distribution inside the porous media close to the steady state at typical saturations $S_w = 0.27$, 0.425, 0.43, and 0.75, respectively, in (a)–(d).
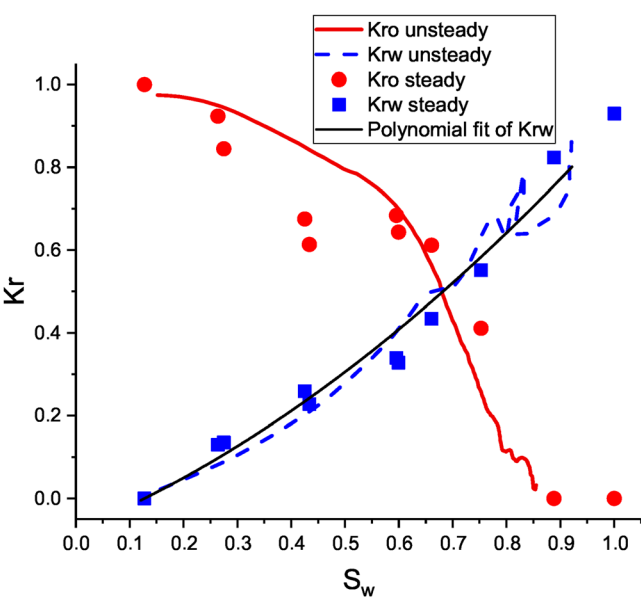

FIG. 5. Relative permeability of oil K_{ro} and water K_{rw} as functions of water saturation S_w. The discrete data points were obtained through steady-state simulations, while the curves represent results from the unsteady-state method (constant-q policy).

almost identical saturation values of $S_w \approx 43\%$ inside the porous media at steady state [see Figs. 4(b) and 4(c)].

At $t = 200\,000$, Case A nearly reaches a steady state. The two-phase distribution at steady state in the porous media is shown in Fig. 4(b). The evolution of q_w and q_o, as well as the densities (ρ_o and ρ_w) at $Y = 80$ and $Y = 520$, as functions of time, is shown in Fig. 6.

From Fig. 6(a), we observe that in Case A, both water and oil reach a constant volumetric flow rate at steady state, with approximately $q_w = 0.7809$ and $q_o = 0.6694$. The flux curves are smooth. The average densities of water and oil at the inlet (ρ_w in and ρ_o in) are very close, both approximately $\rho_{in} = 0.5775$. Similarly, the average densities of water and oil at the exit are close, with $\rho_{out} = 0.560$. From the density difference, we can calculate the pressure difference using $\Delta p = c_s^2(\rho_{in} - \rho_{out})$.

However, from Fig. 7(a), we see that in Case B, at steady state, both volumetric flow rates of water and oil oscillate significantly. This can be understood by comparing Fig. 4(b) with $S_w = 0.425$ and Fig. 4(c) with $S_w = 0.43$. In Case B [Fig. 4(c)], the oil distribution near the outlet appears more discrete than in Case A. As a result, the flow flux of the oil oscillates dramatically. This oscillation also contributes to the relatively large measurement error. Hence, even with the same injection ratio, the distribution of phases at the inlet boundary may influence the measured relative permeability, and this effect may depend on the underlying structure of the porous medium.

Our findings show that while the inlet distribution can noticeably alter internal flow patterns and cause oscillations in volumetric flow rates (e.g., Fig. 7), here its effect on the computed relative permeability is relatively minor. For example, in Fig. 5, two cases with nearly the same water saturation ($S_w \approx 0.25$) exhibit different oil relative permeabilities (K_{ro}), as indicated by the two nearby red disks—one around

the 30 narrow channels for both cases are shown in Table II. The letters "B" and "R" represent water and oil, respectively. It is clear that the phase distributions in the inlet channels differ significantly between Case A and Case B. Despite these differences, both cases result in

TABLE II. The phase distributions at the inlet for cases with $S_w \approx 43\%$ (B: water, R: oil).

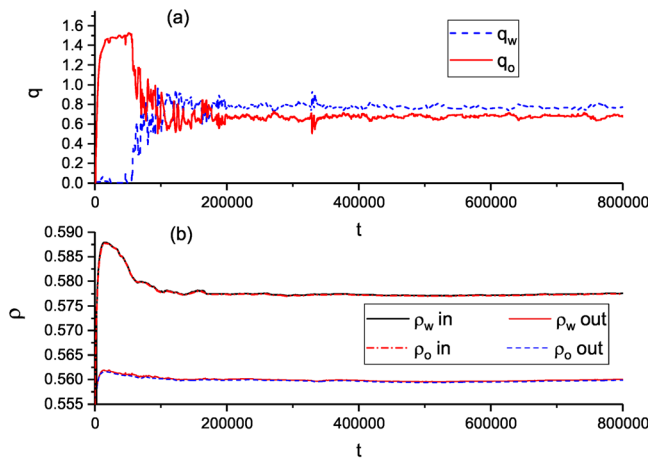| Case	Distributions of inlet channels	Inlet number (B:R)
A	B B B B R R B B R R R B B B R R R B B B R R B B R R R R B B	16:14
B	B B B R R B B B R B R R B R B R B R B B B R R B B R R B B R R	16:14

FIG. 6. Result of Case A. (a) Volumetric flow rate of water (q_w) and oil (q_o) as functions of time step at exit ($Y = 80$), (b) average densities of water and oil at the inlet ("ρ_w in" and "ρ_o in" at $Y = 520$) and outlet ("ρ_w out" and "ρ_o out" at $Y = 80$) as functions of time.

0.84 and the other around 0.93—highlighting the impact of spatial distribution at the inlet. The two cases differ in K_{ro} by about 10% due to different inlet configurations. A similar difference is observed at $S_w \approx 0.4$. Overall, spatial variations at the inlet may cause moderate deviations but do not significantly impact the accuracy of relative permeability results here.

B. Unsteady-state measurement

The unsteady-state method for determining oil–water relative permeability is based on the Buckley–Leverett theory, which describes the one-dimensional advancement of a two-phase waterflood front. It assumes uniform oil and water saturation across any cross section of the rock sample. Initially, the rock sample is saturated with water, and
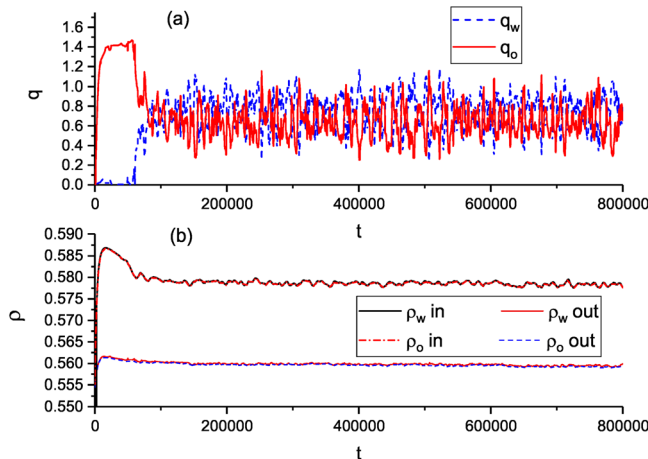

FIG. 7. Result of Case B. (a) Volumetric flow rate of water (q_w) and oil (q_o) as functions of time step at exit ($Y = 80$), (b) average densities of water and oil at the inlet (ρ_w in and ρ_o in at $Y = 520$) and outlet (ρ_w out and ρ_o out at $Y = 80$) as functions of time.

oil is injected to displace the water until only irreducible water remains. Unlike the steady-state method, the unsteady-state method does not involve the simultaneous injection of two fluids into the core. Instead, the oil-saturated rock sample, containing irreducible water, is subjected to waterflooding. During this process, the distribution of oil and water saturation within the porous medium varies with both distance and time, which characterizes the unsteady-state process. Depending on the simulation conditions, either constant pressure difference (constant-Δp) or constant rate (constant-q) waterflooding experiments are conducted on the reservoir rock sample. The production rates of each fluid and the pressure difference across the sample are recorded at the outlet as functions of time.

1. "Constant-q" policy

To neglect the effects of capillary pressure, when using the constant-q policy, the flow velocity should be sufficiently high. We propose a normalized parameter, π_q, to assess this condition, with the criterion given by

$$\pi_q = \frac{A \sigma_{ow} \sqrt{K\phi}}{\mu q L} < 0.6. \tag{28}$$

Here, σ_{ow} is the oil–water interfacial tension, and ϕ is the porosity of the porous media. In our case, $A = 400$ lu and the distance between the upper and lower "pressure sensors" is $L = 440$ lu. Assuming an inlet velocity of 0.004 lu/ts, the flow flux at the inlet is approximately $q = 0.004 \times 400 \approx 1.6$ lu²/ts. In our simulations, we estimate $\pi_q = \frac{400 \times 0.003 \sqrt{48.4 \times 0.77}}{\frac{2}{9} \times 0.1667 \times 1.6 \times 440} \approx 0.11 < 0.6$.

The oil and water relative permeabilities using the unsteady-state method are calculated as follows:

$$f_o(S_w) = \frac{d\overline{V_o}(t)}{d\overline{V}(t)}, \tag{29}$$

$$K_{ro} = f_o(S_w) \frac{d[1/\overline{V}(t)]}{d[1/I\overline{V}(t)]}, \tag{30}$$

$$K_{rw} = K_{ro} \frac{\mu_w}{\mu_o} \frac{1 - f_o(S_w)}{f_o(S_w)}, \tag{31}$$

where $f_o(S_w)$ is the oil saturation and $\overline{V_0}(t)$ and $\overline{V}(t)$ are the normalized cumulative oil and liquid production, respectively, expressed as a multiple of pore volume. Here, K_{ro} and K_{rw} are the oil and water phase relative permeability, respectively; I is relative injectivity, also known as the flow capacity ratio. In the above equation, $q(t)$ is the liquid production rate at the outlet face of the core sample at time t, for constant rate tests, $q(t) = q_0$ and q_0 is the initial liquid production rate at the outlet face of the core sample. Here, Δp_0 is the initial driving pressure difference and $\Delta p(t)$ is the displacement pressure difference at time t, for constant pressure tests, $\Delta p(t) = \Delta p_0$. The relative injectivity I is defined to quantify the intake capacity which varies with cumulative injection

$$I = \frac{q(t)}{q_o} \frac{\Delta p_o}{\Delta p(t)}. \tag{32}$$

From a physical viewpoint, the relative injectivity may be defined as the ratio of the intake capacity at any given flood stage to the intake
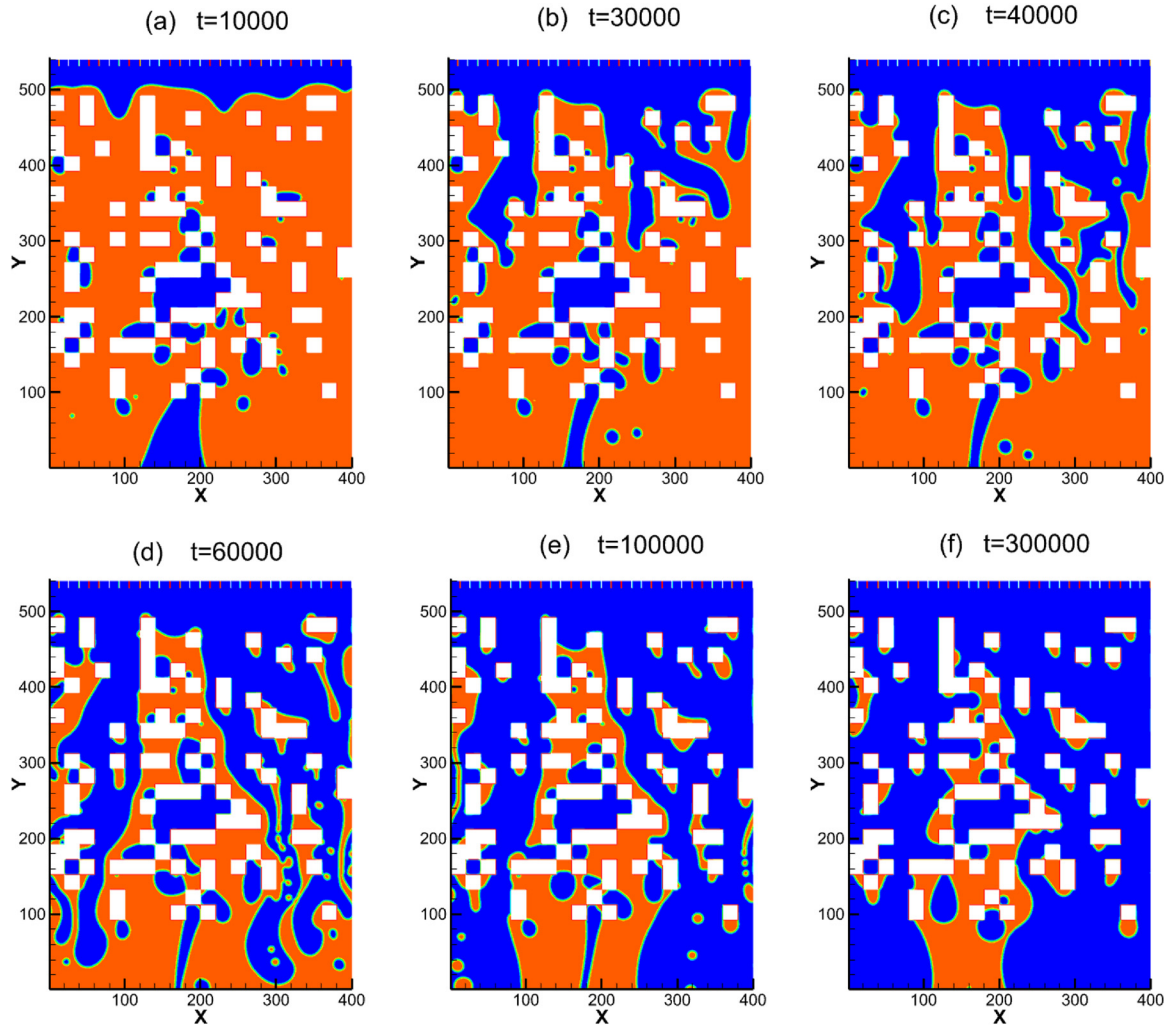
FIG. 8. Evolution of two-phase flow inside the porous media after waterflooding. In the constant-q method, water (blue) is injected at a constant rate into the porous media, which was initially flooded with oil (red), leaving only irreducible water behind.

capacity of the system at the very initiation of the flood (at which moment practically only oil is flowing through the system).

The water saturation at the outlet face of the core sample S_{we} can be calculated through

$$S_{we} = S_{ws} + \overline{V_o}(t) - \overline{V}(t)f_o(S_w), \tag{33}$$

where S_{ws} is the irreducible water saturation.

The simulated waterflooding procedure is shown in Fig. 8. As seen in the figure, at $t = 10\,000$ ts, oil begins to invade the porous media. Even by $t \approx 40\,000$ ts, the oil front has not yet reached the location $Y = 80$. As the waterflooding continues, the oil is progressively displaced, and by $t = 300\,000$ ts, only small oil residues remain inside some narrow pores. The relative permeabilities obtained using the constant-q method are shown in Fig. 5, and the results appear to be consistent with those obtained from the steady LBM simulations.

We now discuss how to determine Δp_0 and q_0 in the relative injectivity formula I, which are critical for obtaining K_{ro} and K_{rw}.

The evolution of the pressure drop (or $\Delta\rho$) and flow flux (q) during the waterflooding process is shown in Fig. 9. As observed, $\Delta\rho$ initially increases, then decreases dramatically, and eventually levels off at a plateau with $\Delta\rho \approx 0.0106$ mu/lu^2. The peak of $\Delta\rho$ occurs at $t \approx 15\,000$ ts (see the dotted line). Similarly, the total liquid flux q increases quickly during the first $15\,000$ time steps, reaches a small peak, and after $70\,000$ steps, stabilizes at a plateau with $q \approx 1.51$ lu^2/ts. In the LBM simulation of flow with an inlet velocity boundary condition, pressure is gradually established, and at the peak value, we assume that the pressure drop is almost fully developed. Therefore, for our calculation of K_{ro} and K_{rw}, we adopt $\Delta\rho_0 = 0.026\,61$ mu/lu^2 and $q_0 = 1.48$ lu^2/s. We conclude that the initial pressure drop (Δp_0) and flow flux (q_0) in the LBM simulation should correspond to the peak of Δp when the pressure drop has been established.

It is also worth noting that in the constant-q policy, the flow flux q stabilizes at a value of $q = 1.51$ lu^2/ts, which is close to the specified
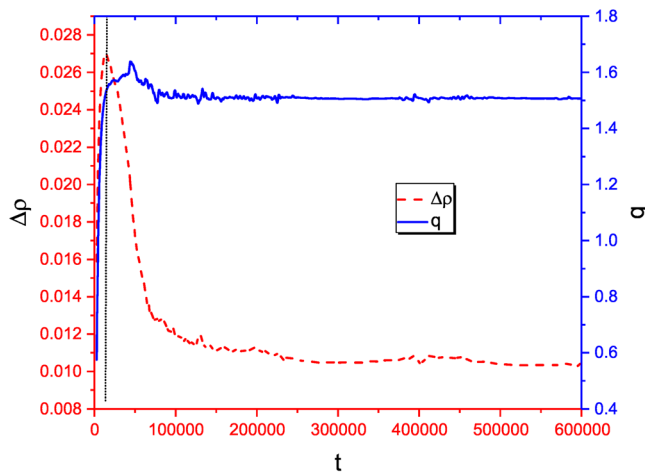
FIG. 9. Density difference ($\Delta\rho$) between the inlet and outlet, along with the total volumetric flow rate of liquid ($q = q_o + q_w$), as functions of the time step at the exit ($Y = 80$) in simulations with constant-q. The pressure drop between the inlet and outlet can be calculated as $\Delta p = c_s^2 \Delta\rho$.

flow flux of $q = 0.004 \, \text{lu/ts} \times 400 \, \text{lu} = 1.6 \, \text{lu}^2/\text{ts}$. The small discrepancy may arise from the confinement of the 30 small inlet channels.

We aim to analyze the evolutionary characteristics of K_{ro}. Before the oil front reaches $Y = 80$ (i.e., $t < 50\,000$), according to the definition of oil saturation [Eq. (29)], $\overline{V}(t) = \overline{V_o}(t)$, meaning that $f_o = 1$ for $t < 50\,000$. Based on the definition of K_{ro} [Eq. (30)], we have

$$K_{ro} = f_o \frac{d\left(\dfrac{1}{\overline{V}(t)}\right)}{d\left(\dfrac{1}{I\overline{V}(t)}\right)}.$$

Thus, for $t < 50\,000$, the relative injectivity I is the sole factor determining K_{ro}. Since $I = \dfrac{q(t)}{q_o} \dfrac{\Delta p_o}{\Delta p(t)}$, it depends on $q(t)$ and $\Delta\rho$. We have
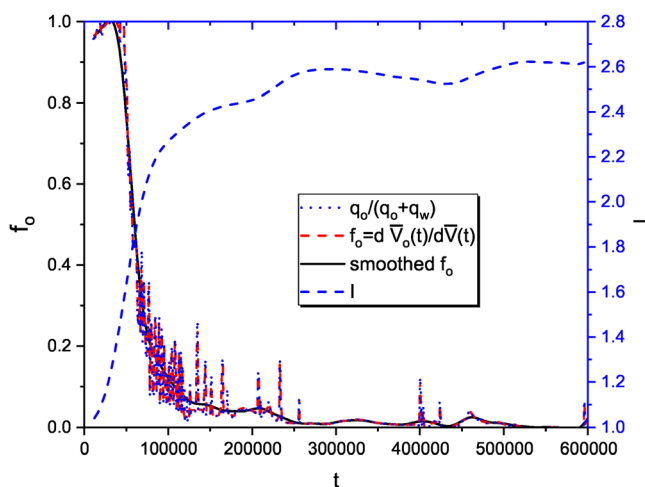
plotted $q(t)$ and $\Delta\rho$ as functions of time in Fig. 9. It can be observed that when $t \in (15\,000, 50\,000)$, $q(t)$ remains almost constant, while $\Delta\rho$ decreases dramatically. Consequently, the relative injectivity I increases sharply from 1.0 to 1.7 during this period (see Fig. 10). During this time, K_{ro} decreases from 1 to 0.71 at $t = 50\,000$ with $S_w = 0.59$.

The oil saturation at the exit, f_o, decreases significantly from 1 at $t = 50\,000$ to 0.03 at $t = 150\,000$. The variation in K_{ro} during this period is largely governed by the variation in $f_o(S_w)$. Therefore, we conclude that initially ($t < 50\,000$), the variation in K_{ro} is determined by $\dfrac{d(\frac{1}{\overline{V}(t)})}{d(\frac{1}{I\overline{V}(t)})}$, with the relative injectivity I being the dominant factor. However, when $t > 50\,000$, the variation in I becomes smoother, and K_{ro} decreases significantly with f_o.

In the following, we will discuss which water saturation should be used to plot the relative permeability curves. There are two possible saturations to consider. One is the saturation at the exit, which is calculated using Eq. (33): $S_{we} = S_{ws} + \overline{V_o}(t) - \overline{V}(t)f_o(S_w)$. The other is the actual water saturation inside the porous media, which is calculated as: $S_w = S_{ws} + \overline{V_o}(t)$.

Figure 11 shows the water saturation inside the porous media (S_w) and water saturation at the exit of the porous media (S_{we}) as functions of time under the constant-q simulation. It is observed that S_{we} is slightly delayed compared to S_w. This can be explained as follows: before the water front reaches the exit (e.g., at $t = 40\,000$), many pores have already been occupied by water, and S_w has increased to ~ 0.5. However, at the exit, only oil flows out, so according to Eq. (33), $S_{we} = S_{ws} = 0.127$ (see Figs. 11 and 8). Therefore, S_{we} lags behind S_w.

In general, we should use the water saturation inside the porous media, i.e., S_w, to plot the relative permeability curve. The plot of oil relative permeability K_{ro} as a function of S_w in Fig. 5 shows good agreement with the data obtained from steady-state simulations (indicated by the red disks). However, if K_{rw} is plotted as a function of S_w, we obtain the blue line in Fig. 12. It is evident that there is a large discrepancy between this curve and the data (blue blocks) from steady-state simulations. In fact, K_{rw} should be plotted as a function of S_{we} rather
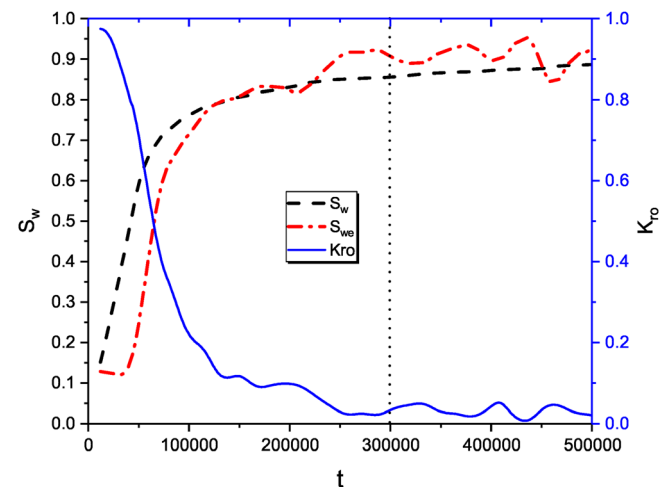

FIG. 10. Oil fraction (f_o) as a function of time (t) and relative injectivity (I) as a function of time (t).

FIG. 11. Water saturation within the porous media (S_w), water saturation at the exit (S_{we}), and K_{ro} as functions of time under the constant-q policy.
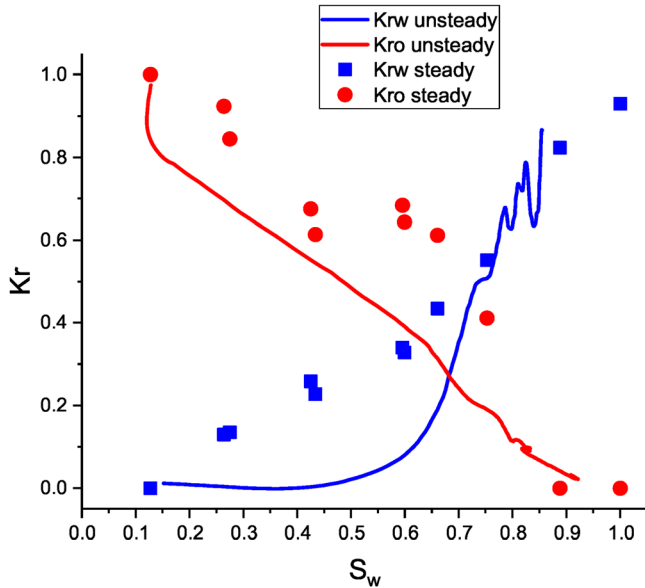
FIG. 12. Applying an inappropriate S_w, relative permeability of oil (K_{ro}) and water (K_{rw}) as functions of (S_w). Discrete data points were obtained from steady-state simulations, while the curves represent results from the unsteady method (constant-q).

than S_w because the calculation of K_{rw} is based on the flow at the exit surface. Further details on this will be discussed below.

According to Eq. (31), we have

$$\frac{1 - f_o(S_w)}{f_o(S_w)} = \frac{K_{rw}/\mu_w}{K_{ro}/\mu_o}. \tag{34}$$

In this equation, f_o should be a function of S_{we} rather than S_w because f_o is derived from the volume flow rates of water and oil at the exit. Specifically, from Eq. (29), we have: $f_o(S_w) = \frac{d\overline{V_0}(t)/dt}{d\overline{V}(t)/dt} = \frac{q_w}{q_w + q_o}$. As shown in Fig. 10, the red dashed line is identical to the dotted line, meaning that $f_o = \frac{d\overline{V_o}(t)}{d\overline{V}(t)}$ is equivalent to $\frac{q_w}{q_w + q_o}$ at the exit.

It is also observed that the $f_o(S_{we})$ curve exhibits some oscillations, particularly around $t \approx 100\,000$ ts, due to the possible discontinuity between the two phases at the exit. Generally, the smoothed f_o curve in Fig. 10 is used for further calculations. Based on Eq. (34), we confirm that K_{rw} is calculated from the flow at the exit and should, therefore, be a function of S_{we}, not S_w.

To generate more accurate relative permeability curves, we need to discard spurious data from the unsteady simulations. From Fig. 11, we can also see that the ranges of S_w and S_{we} are not identical. For example, S_{we} at the exit sometimes exceeds S_w, as seen when $t > 300\,000$ ts. This is reasonable, as the exit may be nearly fully occupied by water at certain moments. However, according to our unsteady simulations, when S_w reaches a maximum of 0.885, with the remaining oil saturation $S_o = 0.115$, the flow of oil inside the porous media stops (i.e., $K_{ro} = 0$). Therefore, any data for K_{ro} when $S_{we} > 0.885$ is not meaningful and should be discarded.

On the other hand, as S_w approaches 0.885, K_{ro} becomes very small, and, according to Eq. (31), K_{rw} should become highly sensitive to f_o. Since the denominator in Eq. (31) is approaching zero, the

calculation of K_{rw} becomes unstable, leading to oscillations. Even small errors in measuring f_o can cause significant errors in K_{rw}. The dashed blue line in Fig. 5, around $S_w \approx 0.85$, illustrates this instability. Therefore, when $S_{we} > 0.885$, the data for both K_{ro} and K_{rw} should be discarded. In Fig. 5, data for $S_{we} > 0.885$ has been omitted.

In conclusion, by plotting K_{ro} as a function of S_w and K_{rw} as a function of S_{we}, and by excluding extraneous data, we can obtain relative permeability curves that are consistent with the results from steady-state LBM simulations.

2. "Constant-Δp" policy

In this subsection, we discuss the measurement of two-phase relative permeability using the unsteady Constant-Δp policy. We aim to maintain a constant inlet pressure in the unsteady "waterflooding" simulation. In our simulations, the surface tension, wettability, and viscosity ratio are consistent with the previously discussed unsteady constant-q case.

At the inlet boundary, a pressure boundary condition is applied, with a constant density $\rho_1 = 0.572$ mu/lu². Initially, the fluid density is set to $\rho_2 = 0.555$ mu/lu². The expected average density at the outlet (located at $Y = 80$) is ρ_2. Consequently, we expect the density difference between the inlet and outlet to be $\Delta\rho = \rho_1 - \rho_2 = 0.017$ mu/lu².

To minimize the effects of capillary forces and end effects in the unsteady simulation, the pressure drop across the porous media must be sufficiently large. A criterion is provided for this judgment. When constant pressure waterflooding is used, the initial displacement pressure difference Δp_0 is determined such that $\pi_p \leqslant 0.6$, where π_p is defined by the following equation:

$$\pi_p = \frac{\sigma_{ow}}{\Delta p_0 \sqrt{K/\phi}}, \tag{35}$$

where Δp_0 is the initial displacement pressure difference. In our simulations, π_p is calculated as

$$\pi_p = \frac{\sigma_{ow}}{c_s^2 \Delta\rho \sqrt{K/\phi}} = \frac{0.003}{\frac{1}{3} \times 0.017\sqrt{48.4/0.77}} \approx 0.067 < 0.6,$$

which satisfies the criterion.

After performing the unsteady simulation and processing the data according to Eqs. (29)–(31), we obtained the oil and water relative permeabilities, K_{ro} and K_{rw}, as functions of S_w (see Fig. 13). The K_{ro} and K_{rw} curves obtained from the unsteady simulation are found to be consistent with the discrete data from the steady simulations.

For the constant. Δp case, we now discuss the details of the simulation, focusing on the trends of the density difference $\Delta\rho$ and flow flux q. The variations of $\Delta\rho$ and q as functions of time are shown in Fig. 14. It can be observed that at the initial time of 2600 time steps, both $\Delta\rho$ and q rapidly evolve toward a quasi-steady state. They then reach plateaus with $\Delta\rho \approx 0.013$ and $q \approx 0.72$. Therefore, in calculating relative injectivity I, we use $\Delta p_0 = c_s^2 \times 0.013$ and $q_0 = 0.72$.

However, it is also noted that after $t = 100\,000$ time steps, $\Delta\rho$ approaches a constant value of approximately $\Delta\rho \approx 0.0117$, which significantly deviates from the expected specified value of 0.017. This discrepancy arises because the convective outlet boundary condition used in the simulation is not a pressure boundary condition, and thus,
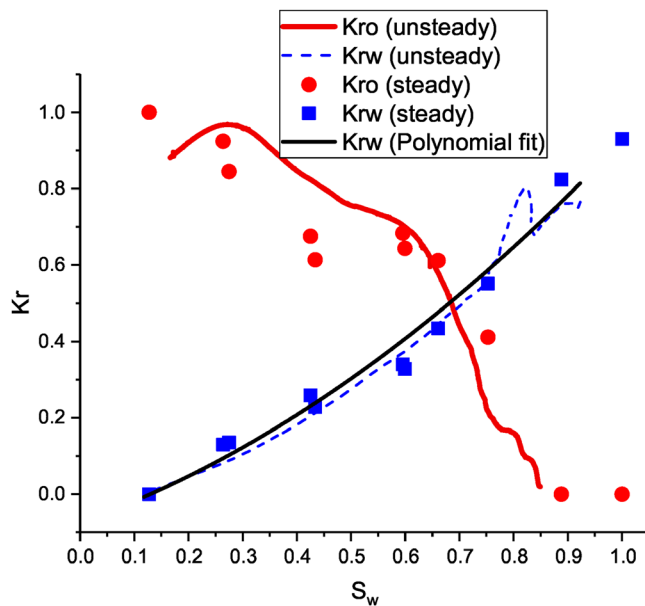
FIG. 13. Oil and water relative permeability K_{ro} and K_{rw}, respectively, as functions of S_w. Discrete symbols were obtained through steady simulations. The curves were obtained through unsteady method (constant-Δp).

it cannot restrict the variation of pressure as effectively as a true pressure boundary condition would.

As a result, in simulations with the constant-Δp policy, the measured Δp shows a notable discrepancy from the expected value, while in the constant-q case, the measured flow flux q remains close to the specified value. Given this, the overall flow characteristics in the constant-q policy are easier to predict. While both constant-Δp and constant-q approaches can yield satisfactory relative permeability curves,

we recommend using the constant-q policy for improved predictability.

III. CONCLUSION

We introduce the first application of the lattice Boltzmann method (LBM) for unsteady-state measurement of two-phase relative permeability curves, removing the restrictions of periodic boundaries. In our unsteady LBM simulations, both the constant-q and constant-Δp policies were employed. By comparing the results with steady-state measurements, we demonstrate that the proposed unsteady-state methods not only yield accurate relative permeability curves but also significantly improve computational efficiency.

In this study, we have analyzed the characteristics of K_{ro} in unsteady simulations. At the early stage of the simulation, $f_o = 1$, and the relative injectivity I is the dominant factor. As the simulation progresses, the variation in I smooths out, and K_{ro} decreases significantly with f_o. While K_{ro} should ideally be plotted as a function of saturation inside the porous media (S_w), since K_{rw} is calculated based on the flow at the exit, it should be expressed as a function of S_{we} rather than S_w.

To obtain an accurate K_{rw} curve, it is crucial to discard spurious data from the unsteady simulations, particularly data corresponding to a remaining oil saturation ($S_w > 0.885$), as this can lead to misleading results.

While both the constant-Δp and constant-q methods yield satisfactory relative permeability curves, we recommend the constant-q approach. This policy is more predictable, as the measured flow flux q aligns closely with the specified value, making it easier to manage the overall flow characteristics in the simulation. In our follow-up studies, we plan to extend the current framework to investigate the effects of varying wetting properties and heterogeneous porous structures in three-dimensional domains.

AUTHOR DECLARATIONS
Conflict of Interest

The authors have no conflicts to disclose.

Author Contributions

Chun Li: Methodology (equal). **Jieming Wang:** Conceptualization (equal). **Youzhi Hao:** Software (equal). **Kun Tu:** Data curation (equal). **Xin Lai:** Data curation (equal). **Haibo Huang:** Methodology (equal).

DATA AVAILABILITY

The data that support the findings of this study are available from the corresponding author upon reasonable request.

REFERENCES

[1]M. M. Honarpour, *Relative Permeability of Petroleum Reservoirs* (CRC Press, 2018).

[2]E. Johnson, D. Bossler, and V. N. Bossler, "Calculation of relative permeability from displacement experiments," Trans. AIME **216**, 370–372 (1959).
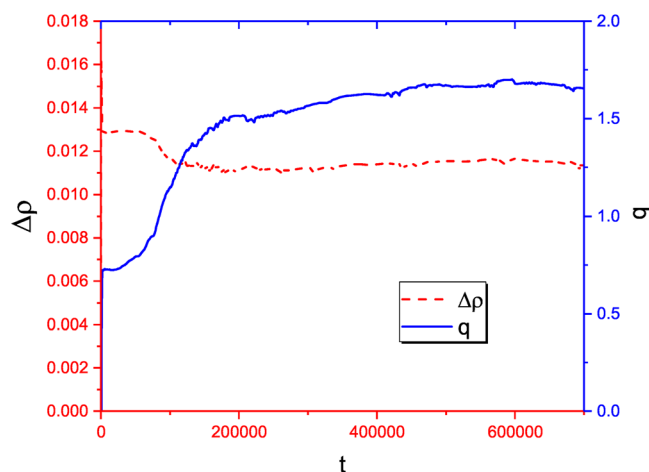
FIG. 14. In the constant-Δp simulation, the inlet and outlet density difference ($\Delta \rho$) and the volumetric flow rate of the liquid ($q = q_o + q_w$) as functions of time at the exit ($Y = 80$). The pressure drop between the inlet and outlet is given by $\Delta p = c_s^2 \Delta \rho$.

04 August 2025 21:49:09

[3]S. E. Buckley and M. Leverett, "Mechanism of fluid displacement in sands," Trans. AIME **146**, 107–116 (1942).

[4]S. Jones and W. Roszelle, "Graphical techniques for determining relative permeability from displacement experiments," J. Pet. Technol. **30**, 807–817 (1978).

[5]H. Huang, M. Sukop, and X. Lu, *Multiphase Lattice Boltzmann Methods: Theory and Application* (John Wiley & Sons, 2015).

[6]A. D. Angelopoulos, V. N. Paunov, V. N. Burganos, and A. C. Payatakes, "Lattice Boltzmann simulation of nonideal vapor-liquid flow in porous media," Phys. Rev. E **57**, 3237 (1998).

[7]M. C. Sukop and D. T. Thorne, *Lattice Boltzmann Modeling: An Introduction for Geoscientists and Engineers* (Springer, Berlin, 2005).

[8]K. Langaas and P. Papatzacos, "Numerical investigations of the steady state relative permeability of a simplified porous medium," Transp. Porous Media **45**, 241–266 (2001).

[9]C. Pan, M. Hilpert, and C. T. Miller, "Lattice-Boltzmann simulation of two-phase flow in porous media," Water Resour. Res. **40**, W01501, https://doi.org/10.1029/2003WR002120 (2004).

[10]J. F. Chau and D. Or, "Linking drainage front morphology with gaseous diffusion in unsaturated porous media: A lattice Boltzmann study," Phys. Rev. E **74**, 056304 (2006).

[11]H.-B. Huang and X.-Y. Lu, "Relative permeabilities and coupling effects in steady-state gas-liquid flow in porous media: A lattice Boltzmann study," Phys. Fluids **21**, 092104 (2009).

[12]D. H. Rothman and J. M. Keller, "Immiscible cellular-automaton fluids," J. Stat. Phys. **52**, 1119–1127 (1988).

[13]A. K. Gunstensen, D. H. Rothman, S. Zaleski, and G. Zanetti, "Lattice Boltzmann model of immiscible fluids," Phys. Rev. A **43**, 4320 (1991).

[14]M. Latva-Kokko and D. H. Rothman, "Static contact angle in lattice Boltzmann models of immiscible fluids," Phys. Rev. E **72**, 046701 (2005).

[15]H.-H. Liu, A. J. Valocchi, and Q.-J. Kang, "Three-dimensional lattice Boltzmann model for immiscible two-phase flow simulations," Phys. Rev. E **85**, 046309 (2012).

[16]S. Leclaire, M. Reggio, and J.-Y. Trépanier, "Numerical evaluation of two recoloring operators for an immiscible two-phase flow lattice Boltzmann model," Appl. Math. Model. **36**, 2237–2252 (2012).

[17]T. Reis and T. N. Phillips, "Lattice Boltzmann model for simulating immiscible two-phase flows," J. Phys. A: Math. Theor. **40**, 4033 (2007).

[18]J. Tölke, "Lattice Boltzmann simulations of binary fluid flow through porous media," Philos. Trans. R. Soc., A **360**, 535–545 (2002).

[19]P. Lallemand and L.-S. Luo, "Theory of the lattice Boltzmann method: Dispersion, dissipation, isotropy, Galilean invariance, and stability," Phys. Rev. E **61**, 6546 (2000).

[20]H.-B. Huang, J.-J. Huang, and X.-Y. Lu, "Study of immiscible displacements in porous media using a color-gradient-based multiphase lattice Boltzmann method," Comput. Fluids **93**, 164–172 (2014).

[21]E. S. Boek and M. Venturoli, "Lattice-Boltzmann studies of fluid flow in porous media with realistic rock geometries," Comput. Math. Appl. **59**, 2305–2314 (2010).

[22]C. J. Landry, Z. T. Karpyn, and O. Ayala, "Relative permeability of homogenous-wet and mixed-wet porous media as determined by pore-scale lattice Boltzmann modeling," Water Resour. Res. **50**, 3672–3689, https://doi.org/10.1002/2013WR015148 (2014).

[23]J.-W. Huang, F. Xiao, and X.-L. Yin, "Lattice Boltzmann simulation of pressure-driven two-phase flows in capillary tube and porous medium," Comput. Fluids **155**, 134–145 (2017).

[24]Z. Lv and H. Huang, "Lattice Boltzmann study of the steady-state relative permeabilities in porous media," Adv. Appl. Math. Mech. **13**, 619–644 (2021).

[25]A. Fakhari, Y.-F. Li, D. Bolster, and K. T. Christensen, "A phase-field lattice Boltzmann model for simulating multiphase flows in porous media: Application and comparison to experiments of co2 sequestration at pore scale," Adv. Water Resour. **114**, 119–134 (2018).

[26]Q. Lou, Z.-L. Guo, and B.-C. Shi, "Evaluation of outflow boundary conditions for two-phase lattice Boltzmann equation," Phys. Rev. E **87**, 063301 (2013).

[27]D. Grunau, S. Chen, and K. Eggert, "A lattice Boltzmann model for multiphase fluid flows," Phys. Fluids A **5**, 2557–2562 (1993).

[28]Q.-S. Zou and X.-Y. He, "On pressure and velocity boundary conditions for the lattice Boltzmann BGK model," Phys. Fluids **9**, 1591–1598 (1997).

[29]O. Aursjø, G. Løvoll, H. A. Knudsen, E. G. Flekkøy, and K. J. Måløy, "A direct comparison between a slow pore scale drainage experiment and a 2D lattice Boltzmann simulation," Transp. Porous Media **86**, 125–134 (2011).

[30]R. Lenormand, E. Touboul, and C. Zarcone, "Numerical models and experiments on immiscible displacements in porous media," J. Fluid Mech. **189**, 165–187 (1988).

04 August 2025 21:49:09